MRI and Ultrasound Imaging of Nanoparticles for Medical Diagnosis

8

Or Perlman and Haim Azhari

Contents

1 Definition of the Topic

Magnetic resonance imaging (MRI) and ultrasound (US) are two prominent medical imaging modalities. They are extensively and routinely used in various medical fields, such as cardiology, embryology, neurology, and oncology. In this chapter we describe the application of nanoparticles for MRI and US image enhancement. Moreover, the utilization of nano-scaled compounds for multimodal MRI-US imaging, allowing further increase of diagnosis certainty, is depicted.

O. Perlman · H. Azhari (✉)
Department of Biomedical Engineering, Technion – Israel Institute of Technology, Haifa, Israel
e-mail: azhari@technion.ac.il

C. S. S. R. Kumar (ed.), *Nanotechnology Characterization Tools for Biosensing and Medical Diagnosis*, https://doi.org/10.1007/978-3-662-56333-5_8

2 Overview

Imaging is a key method for obtaining medical diagnosis. To improve pathology detection ability, intravenous injections of contrast media are often performed. Such materials change a specific physical property of the tissue to which they reach, resulting in improved image contrast.

The developments in the field of nanotechnology have created vast opportunities for improved medical care, in the disciplines of diagnosis and treatment as well. The extremely small nanoparticles' (NPs) size and their high surface area to volume ratio impact various physical properties. This includes mechanical, magnetic, and optical characteristics, as well as allowing improved tumor targeting.

Here, we describe the utilization of NPs in two imaging modalities: US and MRI. These two modalities provide a vast spectrum of clinical applications, are extensively used, and are both non-ionizing in nature. The comparison and added value of NPs over conventional contrast agents will be described herein with an up-to-date review of relevant research. Finally, nano-scaled compounds allowing multimodal MRI-US will be reviewed, and future perspective will be given.

3 Introduction

Imaging is a process in which a certain property of an object is mapped to create a representative image. In medicine, several tissue properties are suitable for imaging purposes, such as atomic number in X-ray computed tomography (CT), proton density and spin relaxation in MRI, and acoustic impedance in US [1]. The image can represent an integrated physical property along a certain dimension (e.g., chest image in X-ray) or a cross-sectional slice (as in MRI and CT), depicting the inner structure of the body. In addition, several imaging protocols and image reconstruction techniques allow the representation of three-dimensional (3D) images. In several modalities, such as single photon emission computed tomography (SPECT), positron emission tomography (PET), and X-rays, the acquisition procedure involves the use of ionizing radiation. The two modalities discussed here, MRI and ultrasound are both non-ionizing in nature and considered hazardless.

The use of diagnostic imaging is highly common in the clinic [2], since correct and early detection of pathology has immense impact on prognosis. An essential factor for pathology detection is the existence of sufficient contrast between normal and abnormal tissue. To increase the differentiation ability, contrast agents are frequently used. In certain modalities, administration of contrast materials may reach 50% of all imaging sessions [3]. A common target for contrast enhancement is blood vessels. After an injection of a contrast media intravenously, veins/arteries are highlighted, allowing an improved examination of their condition. Under such conditions, blockages or impaired vessels are more easily detected, as poor contrast agent uptake is clearly visible. Contrast agents are used also in cardiology [4] and gastrointestinal tract disorders detection where contrast agents can also be administered orally [5]. The utilization of contrast agents is naturally of great importance in tumor detection and characterization [6].

The term NPs commonly relate to particles with two or three dimensions of 1–100 nm in size [7, 8]. Nonetheless, this term is also often used for defining size ranges of 10–1000 nm size range [9], 1–50 nm diameter [10], and even less than 1 micron [11]. The remarkable developments and rapid expansion of the field of nanotechnology have brought staggering opportunities to medical imaging.

The prominent advantages that NPs hold include:

1. *Increased passive tumor accumulation ability*. Tumor-related blood vessels are commonly leaky, with pores of minimum 100 nm in size [12], and typically of less than 780 nm in diameter [13]. This characteristic, known as the enhanced permeability and retention (EPR) effect, does not occur in non-pathologic tissues and consequently leads to NPs accumulation in tumors [14]. To achieve increased tumor penetration using the above described mechanism, long circulation time of the NPs is required. This can be obtained by various manners, e.g., by poly (ethylene glycol) (PEG) encapsulation [15] and dextran coating [16].
2. *Active targeting and efficient drug carrying ability*. The high surface-to-volume ratio of NPs can be utilized for efficient conjunction ability to targeting ligands [17], including folic acid [18], insulin, and peptides. In addition, NPs can be conjugated to drugs, with an increased loading capacity [19].
3. *Tunable imaging parameters*. The extremely small size of the NPs yields also unique physical properties, e.g., by quantum mechanics-related effects [20]. Moreover, by controlling the synthesis procedure to yield particles in different sizes and morphologies, the imaging properties can be tuned to allow superior contrast generation [21, 22].

Accordingly, nano-scaled contrast agents are vastly investigated in all imaging modalities used in the clinic [23]. Prominent composites include gold nanoparticles in CT [24], nanobubbles in ultrasound [25], radiolabeled nanoparticles for PET and SPECT [26, 27], and iron oxide nanoparticles in MRI [28].

Another rapidly growing research trend is the exploitation of a single nano-compound for imaging using two or more different modalities. Using such materials, each imaging technique provides its added value, resulting in a more comprehensive evaluation of the pathologic state, and increased diagnosis certainty. Moreover, using a single contrast agent administration for several modalities prevents the physiological stress stemming from multiple dosages [29].

Several review papers have been published covering topics such as nano-scaled ultrasound contrast agents [30], nano-scaled MRI contrast agents [31], and multimodal contrast agents [32]. This chapter provides a unique step-by-step explanation of the physical background behind the mechanism of nanoparticles as contrast agents for MRI and ultrasound. It is structured to gradually add the needed building blocks for introducing the reader to the current state-of-the-art research in the field of multimodal MRI-ultrasound nano-agents. It is directed and oriented to provide a fundamental picture of the MRI and US nano-imaging field and outlines recently published relevant work.

4 Experimental and Instrumental Methodology

4.1 Magnetic Resonance Imaging (MRI)

MRI is an imaging method which utilizes magnetization properties of the studied tissue to generate images. When subjected to a strong magnetic field, some atom nuclei react in response to radio waves transmitted toward them at a specific frequency (termed the "resonance frequency") by absorbing them and then emitting detectable radio waves. This phenomenon is termed "nuclear magnetic resonance (NMR)." In most medical applications, imaging is based on the NMR of the hydrogen nucleus, i.e., a proton.

In order to explain MRI in simple terms, it is preferable to consider a voxel of tissue. Within such a voxel, (which dimensions are typically about one cubic millimeter), there are numerous hydrogen atoms. Each hydrogen proton can be approximated by a positive electric charge which spins around the proton axis. Resulting from this electric loop, a small magnetic field is generated around the hydrogen proton. Each hydrogen proton has its "private" magnetic field aimed at an arbitrary direction in space. Since magnetic fields are directional, they add up like vectors. Thus, in such random distribution of the small magnetic fields of the hydrogen protons, the resultant magnetization of the voxel is nearly zero (neglecting the earth's magnetic field). When placed within the strong magnetic field of the MRI scanner (denoted as B_0) which strength is commonly between 0.1 and 7 [Tesla] (one Tesla is about 20,000 times the magnetic field of the earth), these numerous magnetic fields are aligned with the MRI field, somewhat similar to a compass needle aligning with the magnetic field of earth. As a result, the voxel becomes "magnetized" with a magnetic moment per volume denoted as M_0 (see Fig. 8.1). This magnetic moment linearly depends on the strength of the magnetic field B_0 and the number of hydrogen protons per volume (termed "proton density").

Next, consider the magnetization vector M_0 of that voxel. This vector is positioned along the z-axis of a stationary frame of reference, which aligns with the magnetic

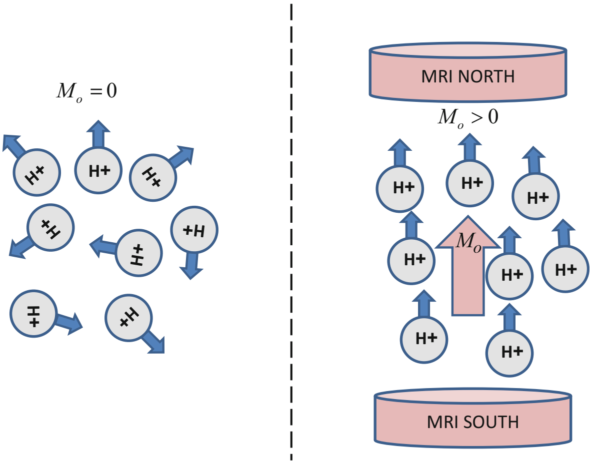

Fig. 8.1 (Left) The magnetic fields of the hydrogen protons in a voxel are randomly oriented in space; hence, the resulting magnetic moment is nulled. (Right) When placed within the MRI, they reorient and the resulting magnetic moment is M_0

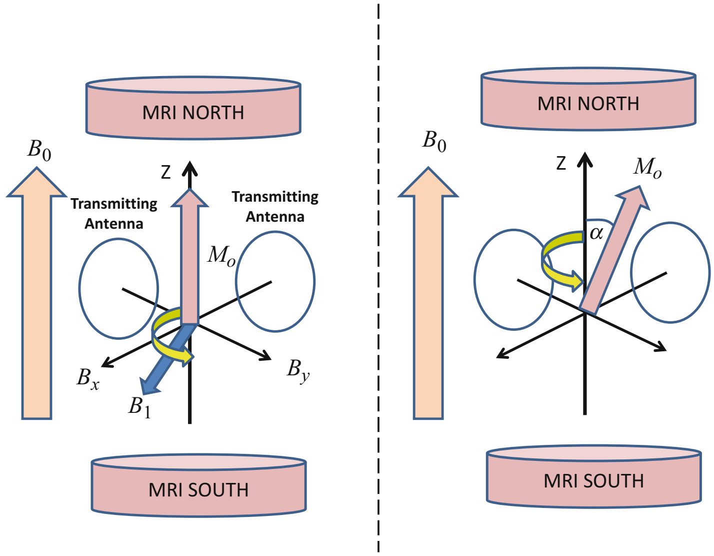

Fig. 8.2 (Left) When two orthogonal antennas transmit radio waves as explained in the text, a B_1 field which rotates about the z-axis at the resonance frequency is generated. (Right) As a result, the magnetization vector M_0 is tilted by an angle α from the z-axis

field of the MRI, i.e., B_0. Two transmission antennas are then positioned along the corresponding x and y axes. The first antenna transmits a field $B_x = B_1 \cdot \cos(\omega_0 t)$ while the second transmits a field $B_y = B_1 \cdot \sin(\omega_0 t)$. This results in a magnetic field B_1 which is located at the x-y plane and rotates around the z-axis with an angular frequency ω_0 which equals to the resonance frequency. This causes a tilt of the voxel magnetization vector M_0 by an angle α from the z-axis (see Fig. 8.2). The magnitude of this angle depends on the strength of the field B_1 and the transmission duration.

When the B_1 transmission is stopped, the tilted magnetization vector M_0 retains its rotation but also begins a realignment process with the z-axis. M_0 has two components: M_z which is aligned with the MRI magnetic field B_0 and M_{xy} which rotates perpendicularly to that field, i.e., in the x-y plane. The rotation frequency is the resonance frequency ω_0. Next, the two transmission antennas are replaced by receiving antennas with the same configuration as shown in Fig. 8.2. Since M_{xy} is actually a rotating magnetic field, it induces currents/voltage in the receiving antennas. These are the signals from which the MRI image is generated.

The contrast in an MRI image is generated by the differences in the signals emitted from the different voxels at a specific acquisition time. This specific time point is designated as echo time (TE). The differences between different materials or tissue types stem mainly from three characteristic properties: (i) proton density which relates to the number of hydrogen protons in the voxel, (ii) spin-lattice relaxation which relates to the realignment of the magnetization vector with the z-axis (see Fig. 8.3) and is characterized by a time constant T_1, and (iii) spin-spin

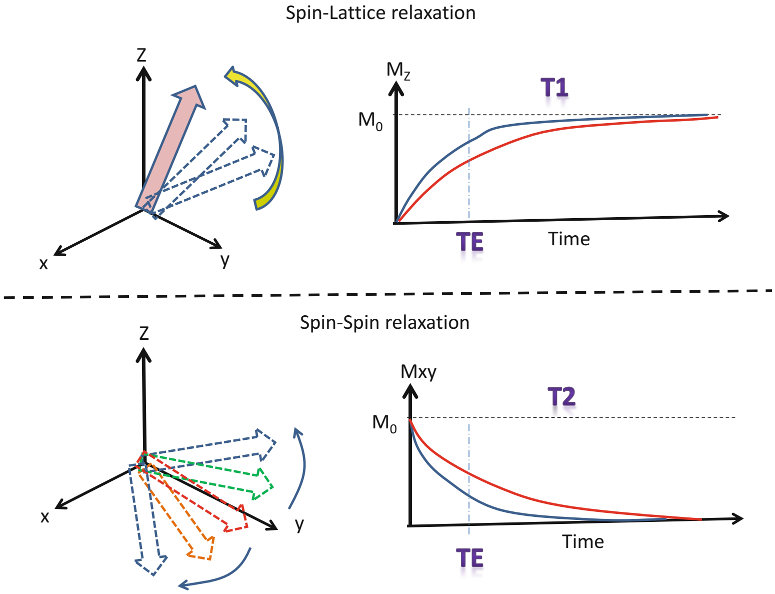

Fig. 8.3 (Top left) Spin-lattice relaxation. (Top right) The response of the vertical magnetization component M_z is time dependent and differs for each material. (Bottom left) Spin-spin relaxation. (Bottom right) The response of the transverse magnetization component M_{xy} is time dependent and differs for each material

relaxation which relates to the dephasing of the transverse magnetization M_{xy} components (see Fig. 8.3) and is characterized by a time constant T_2.

Images are generated by using special spatial encoding magnetic fields called "gradients." The process of image data acquisition is termed "pulse sequence." There are numerous pulse sequences; each sequence emphasizes a different property of the tissue. If the image emphasizes the number of protons per volume, it is termed "proton density weighted." And similarly there are T1- or T2-weighted images.

Two exemplary preclinical MRI scanning systems are depicted in Fig. 8.4, along with a typical mouse positioning MRI cradle.

4.2 Ultrasonic Imaging

Ultrasonic waves are actually sound waves which frequency exceeds 20 KHz (the upper limit for the human ear). Commonly, the frequencies used for medical imaging are in the lower MHz range, i.e., 1–10 MHz. These waves carry mechanical energy which travels at the speed of sound through matter. Typically, in soft tissues, the speed of sound is about 1500 [m/s]. The variations in the speed of sound can be used to characterize and image different tissue types.

Fig. 8.4 (Top left) Preclinical 1 T MRI system (Aspect, Israel), composed of a permanent magnet. (Top right) Preclinical 9.4 T MRI system (Bruker, Germany). (Bottom) Bruker MRI compatible mouse positioning bed. Anesthesia is provided using a chamber into which the mouse head is inserted. The bed is heated to a user-defined temperature, and respiration can be monitored by placing a sensor close to the mouse chest

Sound waves stem from a rapid change in the local pressure at their origin and carry their energy as a perturbation in the medium pressure. Accordingly, their amplitude is measured in pressure units, i.e., Pascal. When traveling through a homogeneous medium, ultrasonic waves are attenuated exponentially with a characteristic attenuation coefficient α. Thus, if the initial amplitude is P_0, at a distance x from the origin, the amplitude will be:

$$P(x) = P_0 \cdot e^{-\alpha x} \tag{8.1}$$

The attenuation coefficient varies from one tissue type to another; therefore, α can be used for tissue characterization and as a source of contrast in imaging as well. Importantly, the attenuation coefficient increases in the lower MHz range almost linearly. Consequently, when the frequency is increased, the penetration range into the tissue decreases rapidly.

Another important tissue property that is relevant to imaging is termed the "acoustic impedance." Marked as Z, it is defined by the multiplication of the tissue density ρ by its speed of sound C, i.e.:

$$Z = \rho \cdot C \tag{8.2}$$

When traveling from one tissue to another, the ultrasonic waves encounter a change in the acoustic impedance. As a result an echo is generated. The ratio between the echo amplitude P_R and the amplitude of the impinging wave P_I is called the reflection coefficient R and is given by:

$$R = \frac{P_R}{P_\mathrm{I}} = \frac{Z_2 - Z_1}{Z_2 + Z_1} \tag{8.3}$$

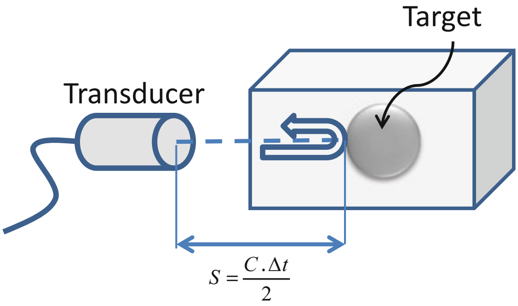

Fig. 8.5 Ultrasonic waves transmitted from the transducer will be reflected from a target having different acoustic impedance. The echo amplitude depends on the reflection coefficient, and the distance is calculated from the travel time of the waves back and forth

where Z_1 and Z_2 are the acoustic impedances of the first and second tissues, respectively. As can be noted, the absolute value of R ranges between 0 and 1; thus, if $Z_2 \gg Z_1 \Rightarrow \mathrm{R} \approx 1$, such as the case for metal implants or bones relative to soft tissues, strong echoes will be reflected. On the other hand, one can note that also when $Z_2 \ll Z_1 \Rightarrow \mathrm{R} \approx -1$, such as the case for air next to soft tissues or blood, the reflection coefficient is high and strong echoes will be obtained. (The negative sign merely indicates phase change.)

The amplitude P_T of the wave that travels through the boundary between the two tissues into the second one is given by the transmission coefficient:

$$T = \frac{P_T}{P_I} = \frac{2Z_2}{Z_2 + Z_1} \tag{8.4}$$

In most of the cases, ultrasonic imaging is based on measurements of the reflected echoes. The basic principle is depicted schematically in Fig. 8.5. A transducer, which is commonly made of a piezoelectric material, transmits a short ultrasonic wave into the body. The wave travels at the speed of sound C. Whenever it encounters a change in the acoustic impedance (Eq. 8.2), an echo is reflected (Eq. 8.3). The echo travels back to the transducer. Its amplitude and time of arrival Δt are registered. The distance S to the reflection point is estimated using the equation:

$$S = C \cdot \frac{\Delta t}{2} \tag{8.5}$$

To obtain a two-dimensional (2D) image, the acoustic beam sweeps through the object. This is commonly done using a fan-shaped configuration as depicted in Fig. 8.6. At every transmission angle, the echoes reflected from the object along that beam are collected and stored. The time elapsed from the ultrasonic pulse transmission to each detected echo is translated into distance using Eq. 8.5. The 2D location is determined by accounting for the transmission azimuth as well (see Fig. 8.6). The amplitude of the echo is graphically presented by assigning a gray level value to the relevant pixel. The stronger the echo the brighter is the pixel.

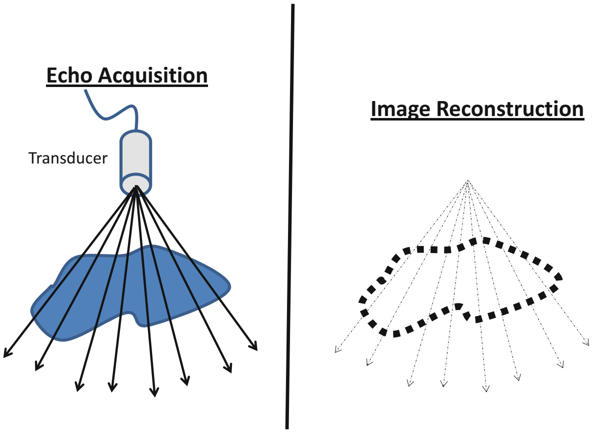

Fig. 8.6 (Left) In order to obtain a 2D image, ultrasonic pulses are transmitted along multiple directions through the object. The echoes reflected along each transmission direction are collected and registered. (Right) An image is reconstructed by depicting each echo as a bright pixel at the corresponding spatial location

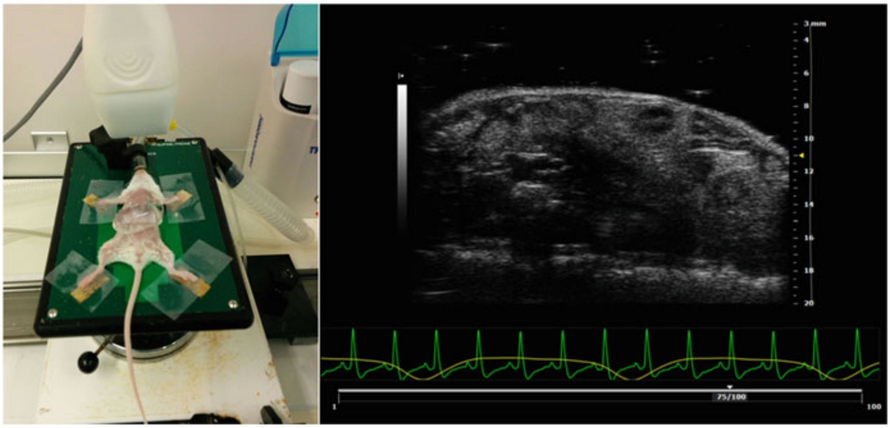

Fig. 8.7 (Left) Mouse positioning and imaging setup (VisualSonics, CA). The limbs are positioned atop electrodes, providing online ECG display. The surface is heated to a user-defined temperature, and anesthesia is applied via a facial mask. The mouse-imaged area is shaved and depilated, and a coupling gel is applied. (Right) A B-mode (reflected waves) ultrasound image of the mouse abdomen scanned using Vevo 2100 high-frequency ultrasound scanner (VisualSonics, CA)

An example of murine in vivo ultrasound experimental setup, as well as a typical pulse-echo (B-scan) image, is shown in Fig. 8.7.

Much less common is the use of through-transmission imaging. With this method, the time required for the ultrasonic waves to travel from one side of the scanned object to another and their amplitudes are registered. From this information two types of images can be generated (see Fig. 8.8): (i) a projection image, which is actually an acoustic shadow of the object, and (ii) a computed tomography (CT) cross-section, which can be reconstructed when collecting projections around the object. The latter is basically similar to X-ray CT images, but the reconstructions map the speed of sound

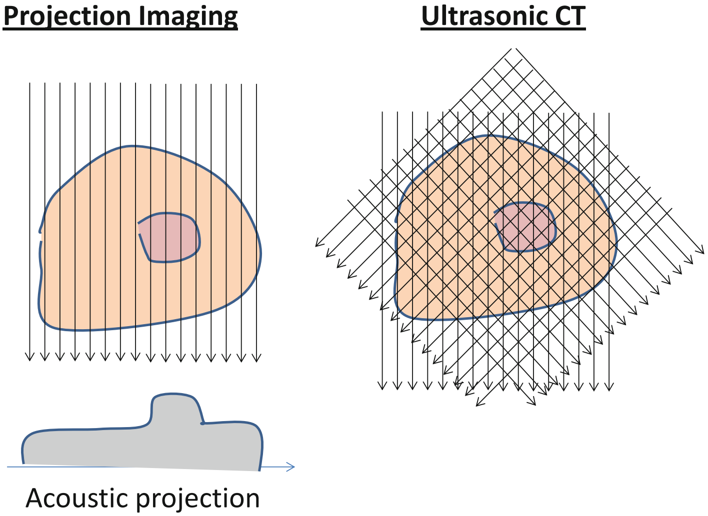

Fig. 8.8 (Left) By measuring the travel times and amplitudes of through transmitted waves, an acoustic projection (shadow) is obtained. (Right) By collecting projections from around the body, a computed tomography (ultrasonic CT) images can be obtained

or acoustic attenuation coefficient. An exemplary dedicated breast scanning system which is based on through-transmission ultrasound is depicted in Fig. 8.9.

5 Key Research Findings

This part will include three major subsections: (i) nanotechnology-based US imaging tools for medical diagnosis, (ii) nanotechnology-based MRI imaging tools for medical diagnosis, and (iii) nano-scaled compounds for multimodal MRI-US imaging. Each subsection begins by describing the main principles of contrast agent enhancement mechanisms relevant to the specific modality, including examples of conventional contrast agents. Next, representative and up-to-date findings (mainly from the years 2010–2016), related to nano-scaled contrast agents, will be described.

5.1 Nanotechnology-Based Ultrasound Imaging Tools for Medical Diagnosis

5.1.1 General Principles of Ultrasound Contrast-Enhancing Mechanism

The conventional contrast agents for ultrasonography are gas-filled microbubbles (MBs), a few microns size. The core can be made of air or other gases such as fluorocarbon and sulfur hexafluoride. The coating can be composed of albumin, a phospholipid shell, a polymer, or other materials aimed to increase the bubbles'

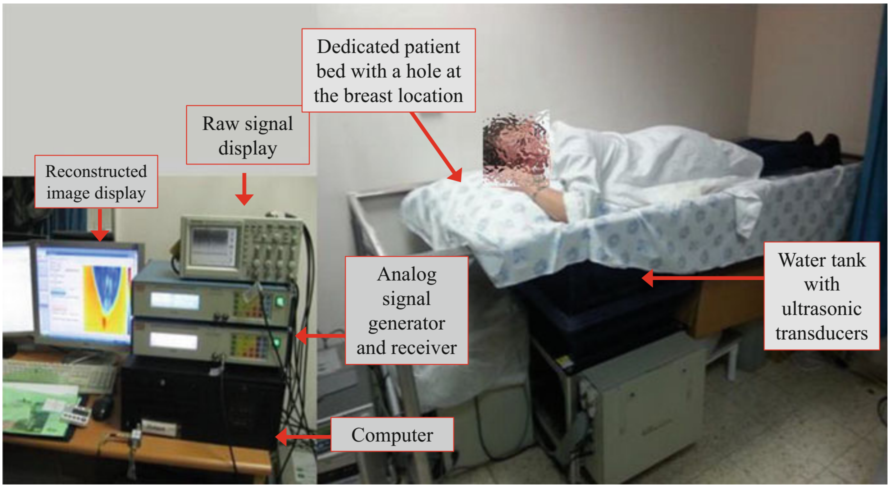

Fig. 8.9 Through-transmission ultrasound system components. (Left) The electronic boxes and computerized elements. (Right) A patient is positioned atop a dedicated bed, with a hole through which the breast is inserted. The examined breast is immersed in a water container, and ultrasonic transducers perform 2D/3D acoustic projection or computed tomography scanning. Generously contributed by Ilana Katz-Hanani from the Technion – Israel Institute of Technology

stability in the vascular system [33]. As the acoustic impedance of the MBs is negligible compared to biological tissues, they are highly echogenic. In other words, the impedance mismatch of the bubble with the blood causes an almost complete reflection of the acoustic energy back to the ultrasonic transducer. Moreover, the bubbles resonate in response to ultrasonic irradiation and yield a nonlinear effect generating subharmonic and higher harmonic signals. To further increase the MBs signal-to-noise ratio (SNR), signal processing means can be implemented on the acquired raw radiofrequency (RF) acoustic signals, for obtaining images depicting specific harmonics only [34]. As the MBs are retained in the blood for several minutes without crossing the endothelium [35], their main clinical application is vascular imaging. In cardiology, MBs can assist in assessing the heart function, improve the visualization of the cardiac chambers' borders, detect thrombus or ischemia, etc. [36]. Vascular flow quantification may also be obtained by MBs destruction. This can be achieved using a high mechanical index pulse transmission [37] and analysis of the refilling rate. Difference in vascular flow characteristics can also assist in tumor detection and evaluation, e.g., in the liver [38].

In attempts to reduce the size of ultrasound contrast agents for obtaining the benefits of the nano-scale, as described in Sect. 3, five major research paths were investigated. In the straightforward approach, a downscaled version of a microbubble is synthesized, i.e., a gas-containing nanobubble. Another approach replaces the gas core with a liquid. Although the liquid content, which is termed nanodroplet, is less echogenic than gas, it can be vaporized into an increasingly echogenic microbubble after tumor penetration. Two additionally attractive methods are the

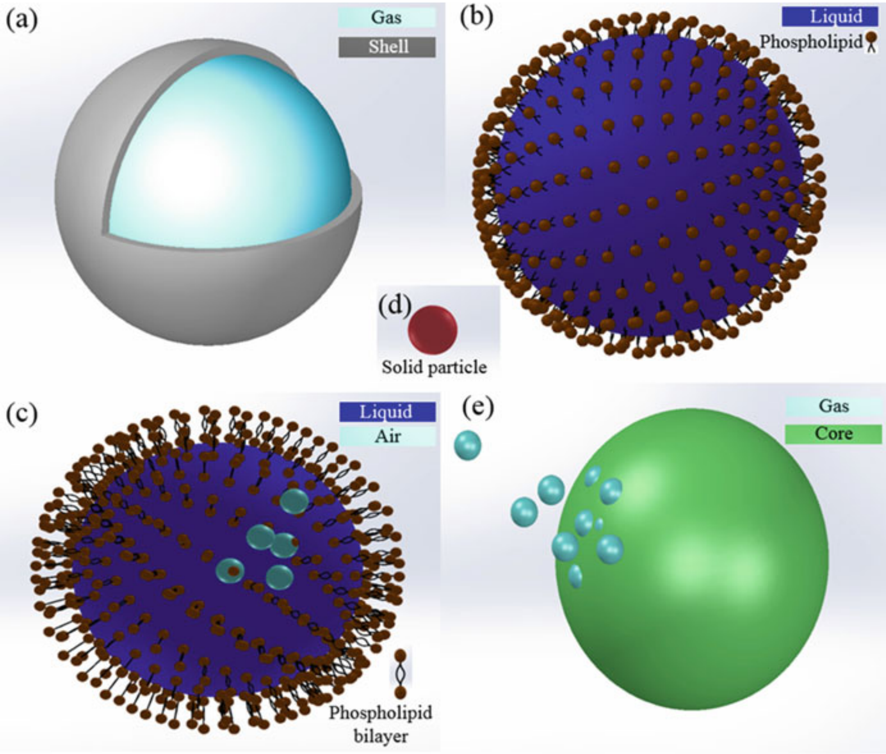

Fig. 8.10 Schematic illustration of nano-scaled ultrasound contrast agents. (**a**) Gas core nanobubble – gas (typically fluorocarbon) is trapped in a polymer or a lipid shell. (**b**) Nanodroplet – a liquid core nanoparticle, which can be vaporized into a gas-containing microbubble. The shell may be a phospholipid layer, as illustrated. (**c**) Echogenic liposome. The echogenicity is assumed to occur from air inside the liquid phase or the lipid bilayer. (**d**) Solid nanoparticle. (**e**) Gas-generating nanoparticle

synthesis of echogenic liposomes and the utilization of gas-generating nano-scaled substances. Finally, attempts to use solid nanoparticles as ultrasound contrast agents were performed. The commonly used nano-structure shells were composed of either a polymer or a single/double layer lipid. Figure 8.10 illustrates the main element of each approach. In the following subsections, we shall further elaborate on each contrast agent type and describe the representative works recently performed.

5.1.2 Gas Core Nanobubbles

As stated earlier, the intuitive way to obtain a nano-scaled US contrast agent is to synthesize a smaller version of a microbubble. When studying the capabilities of aptamer-conjugated nanobubbles (486 nm), ex vivo 40 dB enhancement was demonstrated [39]. It shall be noted that a 40 MHz transducer was used and that the nucleic acid ligands were designed to target human acute lymphoblastic leukemia, while the echogenic core was composed of perfluoropropane (C_3F_8) gas. The necessary question at this point is weather the abovementioned contrast is suitable for in vivo applications and its comparability to conventional agents.

A comparative study between 435 nm C_3F_8-filled nanobubbles and clinically used microbubbles (SonoVue®, for which the average particle size is of 2.5 μm) demonstrated higher contrast improvement and longer imaging duration when using the nanobubbles [40]. This was demonstrated both in vitro and in vivo, using gastric cancer xenograft in mice. A further support for the in vivo ability of C_3F_8-filled nanobubbles was demonstrated in [41], as bubbles of 200–650 nm generated contrast improvement in an in vivo breast tumor mice model. Researchers from the same group have also synthesized similar nanobubbles but with a more uniformly distributed size (478.2 ± 29.7 nm), conjugated to tumor targeting agents [42].

In another mice study [43], gas-containing polymer nanobubbles (521 nm) demonstrated contrast in the kidney, liver, and tumor which was comparable to SonoVue® microbubbles. Moreover, the improved contrast imaging duration was longer in the NPs' case. The NPs' ability to load gene therapy agents and to efficiently transfect them in vitro was better than that of compared liposomes.

Polymers offer a biodegradable, biocompatible, and stable shell choice for nanobubbles. Commonly, the FDA-approved polymer poly(lactic-*co*-glycolic acid) (PLGA) is used [44]. In an in vitro study, 1D ultrasound scans (A-mode) at 10 MHz of PLGA air-filled nanocapsules (370 nm, 45 μg/ml) demonstrated 15 dB signal enhancement [45]. In another study, perfluorocarbon gas-filled PLGA bubbles (approximately 700 nm in diameter) generated contrast improvement when injected to tumor-bearing mice, under harmonic imaging [46].

A formulation of smaller gas-filled nanobubbles (200 nm in diameter), composed of C_3F_8 core, lipid-shelled nanobubbles, with the surfactant pluronic, was reported in [47]. In a later comparative study [48], the echogenicity of these nanobubbles was reported as comparable and in some cases superior to the clinically used Definity® microbubbles.

A unique biological approach was suggested by Shapiro et al. [49], which derived gas vesicles of 45–250 nm width and 100–600 nm length from bacteria and archaea (Fig. 8.11). In vitro studies demonstrated these gas-filled substances' ability to enhance the ultrasonic signal in both the fundamental frequency and higher harmonics. As with microbubbles, the vesicles were destructible using high pressure pulses. Similar to other NPs, aggregation of the vesicles resulted in an increased signal. In vivo mice studies using nontargeted intravenously injected vesicles demonstrated increased liver and inferior vena cava contrast.

5.1.3 Nanodroplets

Nanodroplets are liquid core composites. Although they can be synthesized to a size as small as 200 nm, their echogenicity is lower than gas core NPs [30], due to their reduced compressibility. In order to increase contrast ability, after the NPs accumulate in a cancerous tissue, they can be phase-shifted by vaporization into gas-containing microbubbles. It was demonstrated that acoustic radiation, generated by a 5 MHz transducer, was able to transform decafluorobutane (DFB) nanodroplets of 200–600 nm diameter, into microbubbles [50].

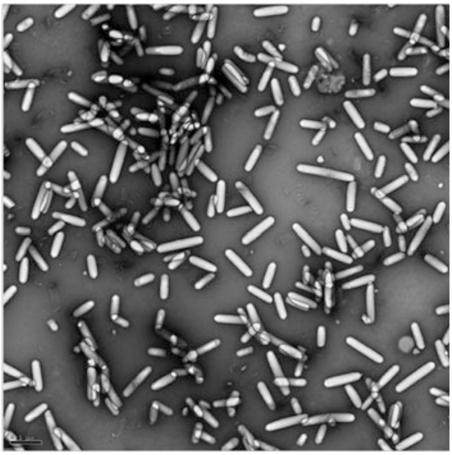

Fig. 8.11 Transmission electron microscopy (TEM) image of purified gas vesicles from *Anabaena flos-aquae*. Generously contributed by Prof. Mikhail Shapiro from California Institute of Technology

In another study, a liquid core of perfluorooctyl bromide (PFOB) was encapsulated in a shell of PLGA, with a PEGylated phospholipid-modified surface [51]. In this work, dosages of 50 mg/mL nanocapsules, 200 μL in volume and 200 nm in size, were injected into gel-containing chambers, intravenously (IV) through the retro-orbital sinus and intratumoral to tumor-bearing mice (human pancreatic cancer cells). Although the in vitro and intratumor experiments demonstrated improved contrast, the IV injections did not result in any improved tumor visualization. While histological studies demonstrated some particles residing in the tumor, the lack of IV injection-related contrast may stem from the relatively big particle size, preventing the accumulation of high particle dosage in the tumor.

A recently developed method enabled the synthesis of a mixed solution containing nanodroplets and gas core nanobubbles [52]. In vitro 15 MHz examination demonstrated that the solution resulted in an improved backscatter compared to liposomes, and in vivo 40 MHz mouse aorta imaging demonstrated clearly visible contrast improvement.

In various cases, the stimulator for the nanodroplets vaporization into microbubbles is diagnostic ultrasound with sufficiently high mechanical index. A spatially specific approach was recently suggested, in which low intensity focused ultrasound was used [53]. The researchers showed that acoustic transmission of 1 MHz focused ultrasound, applied for 2 min at 3.2 W/cm^2 intensity, was able to phase change nanodroplets into microbubbles located in a subcutaneously implanted mice tumor, yielding visibly detectable image brightening. In addition, the conjugation of folate to the nanodroplets (average diameter of 321 nm) resulted in significantly improved tumor targeting ability.

5.1.4 Echogenic Liposomes (ELIPs)

Echogenic liposomes (ELIPs) are phospholipid vesicles that contain gas either in their lipid section or in their liquid center [54, 55]. Compared to gas core NPs, they are more stable and mechanical pressure durable [56]. In an in vitro study, the acoustic characteristics of ELIPs were examined using a broadband stationary pulse-echo methodology [57]. The resulting contrast agent efficiency was at the same range as commercially available microbubbles, when comparing the scattering-to-attenuation ratio. It should be noted that the synthesized ELIPs' solution contained a large number of 65 nm in diameter particles, but the general size distribution was rather wide, containing also particles with a diameter of a few microns.

In another study, a physiological flow phantom containing porcine plasma was used to evaluate ELIPs suitability for blood pool contrast enhancement [58]. Acquired B-mode images indeed detected improved image contrast (mean digital intensity of approximately 20 dB).

A vascular application was suggested for the ELIPs, by using their conjunction to atherosclerosis-related inflammatory markers [59]. The concept was demonstrated in an in vivo porcine study, in which the ELIPs yielded enhanced signal at the diseased artery site, when imaged using intravascular ultrasound (IVUS). In a different study, tissue plasminogen activator (tPA) was loaded into ELIPs, providing dual imaging therapy capabilities [60]. An occlusive thrombus was produced in the aorta of rabbits. The thrombus site was detected using real-time B-scan mode, following the injection of the ELIPs. A 2-min ultrasound transmission with a mechanical index of 0.4 was then performed to release the blood clots breakdown agents. Blood flow velocity recovery was measured using pulsed Doppler. The loaded ELIPs demonstrated a significant image brightening effect as well as faster and more efficient blood flow velocity improvement (indicating the thrombolytic therapy effect).

5.1.5 Gas-Generating Nanoparticles

A different and unique method for generating NP-based US contrast is engineering an agent capable of releasing gas either spontaneously, in a response to specific pathology, or when sensing a clinically important molecule.

Polymeric NPs were demonstrated as potential candidates for such substances. According to the study depicted in [61], carbonate dioxide nanobubbles were formed on the surface of a polymeric nanoparticle. As reported, the bubbles have gradually merged into microbubbles. This potentially should occur at the tumor site, post penetration using the EPR effect. The gas-generating polymeric NPs were 200–500 nm in size, and increased echogenicity was demonstrated using subcutaneous injection to the lower backs of mice, as well as intratumoral injection. The duration of ultrasound signal increase was around 12.5 min, followed by gradual decrease.

In a selectively activated gas release study [62], the researchers synthesized a 500 nm silica core particle, coated by a layer of enzymes that catalyze the decomposition of hydrogen peroxide (H_2O_2) to microbubbles. The clinical importance of H_2O_2 stems from its association with various diseases, including inflammation. The nanospheres were injected near a subcutaneous abscess in rats and generated well-detectable microbubbles.

Recently, a different group of researchers synthesized poly(vanillin oxalate) particles of 550 nm diameter, capable of releasing CO_2 when triggered by H_2O_2 [63]. Since ischemia/reperfusion injury is also associated with H_2O_2 production, the particles were able to detect the injury site by releasing echogenic bubbles in an injured liver mice model. Moreover, the particles released vanillin that demonstrated therapeutic ability.

In another recently published work, a pluronic-based nanocarrier, containing calcium carbonate particles, was reported as suitable for ultrasonic tumor imaging [64]. The complex size was characterized as 160 nm at physiological conditions and was able to generate CO_2. Imaging at 10 MHz frequency demonstrated in vitro echogenicity as well as tumor enhancement in mice 1 h post intravenous injection. Characterization of the gas formation in various pH conditions demonstrated increased efficiency at acidic conditions, which are typical in some tumor cases.

5.1.6 Solid Nanoparticles

Although solid NPs are not expected to cause nonlinear ultrasound phenomena, several attempts were made to examine their suitability to serve as US contrast enhancers. Silica nanospheres of 100 nm were examined using 30 MHz B-scan [65]. Agarose phantom experiments demonstrated the particles visualization, and IV injections of the particles to mice yielded image brightening of the liver. This brightening persisted for 1.5 h. Nevertheless, the average gray-scale change was only around 30%, and the visual effect was rather mild.

Another solid NPs examined for ultrasonography are polylactic acid (PLA) NPs (250 nm diameter) [66]. PLA is a biodegradable, FDA-approved material [67]. The NPs were conjugated to breast cancer cells targeting agents. B-scan images of the PLA-nanoparticles containing cells demonstrated image brightening; however, the obtained effect was of less than 25%.

In a later study, the advantages of solid materials (increased durability over time to ultrasonic radiation as opposed to collapsible bubbles) were incorporated with the high echogenicity of gas-filled substances [68]. Silica and silica-boron perfluoropentane (PFP)-filled nanoparticles were synthesized, with 500 nm in diameter. The NPs were injected into the thighs of rabbits, yielding a well-visualized signal for 4 days. The authors suggested that the ability of the NPs to maintain their location without collapsing for long time periods may be useful for marking and visualizing the borders of breast cancer during surgical procedures.

In a later study by the same group of researchers, 500 nm iron-silica nanoshells were filled with PFP [69]. The particles were visible for 10 days after intratumoral injection in ex vivo breast tissue as well as in mice tumors.

Although the ability to maintain a fixed anatomical location for long time periods is an advantage in the clinical case of surgical-related tumor delineation, it constitutes a disadvantage for the application of systematically administering faster-degrading contrast agents (e.g., for tumor detection). To address this issue, it was suggested to use phosphate-based glass nanospheres (200–500 nm in diameter) [70]. The particles were imbedded in matrigel and injected into mice flanks. The resulting images demonstrated around fourfold signal increase by injecting 2 mg/mL of the composite. In addition, phantom studies showed that the particles imaging life was about 4 h.

Multi-walled carbon nanotubes (20–30 nm diameter, 400 nm length) were investigated as harmonic imaging and B-scan ultrasound contrast agents [71]. The particles brightened the injection region in ex vivo porcine livers and hearts, as well as in in vivo porcine bladder.

Additional studies in which solid-based NPs were investigated for ultrasound imaging include iron oxide and copper oxide NPs. As these two cases involve MRI imaging as well, they are described in the multimodal imaging section (5.3.2).

5.2 Nanotechnology-Based Magnetic Resonance Imaging Tools for Medical Diagnosis

5.2.1 General Principles of MRI Contrast-Enhancing Mechanism

The prevailing mechanism for MRI contrast improvement using exogenous media is relaxation time shortening. The inverse of the longitudinal (spin-lattice) relaxation time r_1:

$$r_1 = \frac{1}{T_1} \quad [\mathrm{ms}]^{-1} \tag{8.6}$$

and the inverse of the transversal (spin-spin) relaxation time r_2:

$$r_2 = \frac{1}{T_2} \quad [\mathrm{ms}]^{-1} \tag{8.7}$$

can be empirically estimated with respect to various particle concentration, yielding a quantitative estimate of the contrast agent ability to shorten the relaxation time (occasionally termed as molar relaxivity), with the units of $[\mathrm{mM}^{-1}\mathrm{s}^{-1}]$.

An ideal T1 contrast agent will have an r_2/r_1 ratio which is close to one [72] and a high r_1 value. On the contrary, the higher the r_2/r_1 ratio is, the more efficient the contrast agent is for T2 imaging [73].

The most prevalent and routinely used contrast agents in clinical MRI are gadolinium-based compounds which shorten the T1 relaxation time of nearby water molecules. This effect thereby yields a brightened region which is termed as "positive contrast." Although the exact longitudinal relaxivity may be different for various products, the characteristic value for these materials is 5 $\mathrm{mM}^{-1}\mathrm{s}^{-1}$ [74]. A known limitation of gadolinium-based agent injection is the possible clinical complication, to which renal disease patients are susceptible. As gadolinium administration to such population may cause nephrogenic systemic fibrosis, it should be highly avoided [75].

Another paramagnetic metal that is used for positive contrast generation is manganese. The application of manganese-based agents to the liver and to the gastrointestinal tract was previously approved for clinical use [76].

Moving to the nano-scale, three main research paths are prevalent in the literature: (i) the implementation of a gadolinium-based nano-composite, as discussed in Sect.

5.2.2; (ii) the use of T1-related contrast agents which are manganese-based NPs, as discussed in Sect. 5.2.3; and (iii) the use of iron oxide nanoparticles (IONPs) which are the most popular NPs in MRI [77, 78], as discussed in Sect. 5.2.4.

Although not the focus of this section, it should be noted that several additional nano-scaled materials, which are not based on the relaxation mechanism of MRI, are increasingly developed. Two main examples are the utilization of non-proton-based imaging. For example, in a mice study utilizing ^{19}F MRI, perfluorocarbon nano-emulsions were targeted to venous thrombosis, resulting in contrast to noise ratio improvement [79]. In another example, nano-scaled chemical exchange saturation transfer (CEST) agent dendrimers, 5 nm in size, presented a significant contrast improvement for over an hour, after injection into mice brain tumors [80].

5.2.2 Gadolinium-Based Nanoparticles

As stated above, the intuitive approach for engineering a nano-scaled MRI contrast agent would be to synthesize a nano-scaled version of a gadolinium-based composite. PEGylated gadolinium oxide (Gd_2O_3) NPs of less than 10 nm were synthesized for cell labeling [81]. Under a magnetic field of 1.41 *T*, the NPs presented a relatively high r_1 relaxivity of 14.2 $mM^{-1}s^{-1}$, while characterized by a close to one (1.21) r_2/r_1 ratio. When brain cancer cells were labeled with the particles, their in vivo detection in mice brains was feasible. The effect of coating on the longitudinal relaxivity of Gd_2O_3 NPs was examined in [82]. It was found that polyvinyl pyrrolidone (PVP) coating yielded a high value of r_1 relaxivity, 12.123 $mM^{-1}s^{-1}$, whereas oleic acid-based coating yielded only 0.5397 $mM^{-1}s^{-1}$. The PVP-coated Gd_2O_3 NPs were later injected to tumor-bearing mice. Although the tumor contrast improvement was not very dominant, the liver blood vessels visualization improved, as well as the kidney contrast.

In another approach, gadolinium molecules were loaded into PEG-coated liposomes of less than 100 nm [83]. The particles yielded an approximately 30% contrast improvement in a murine tumor model, as well as improved liver positive contrast. The synthesis of gadolinium-encapsulated carbon dots (12 nm) resulted in a longitudinal relaxivity of 5.88 $mM^{-1}s^{-1}$ at 7 T [84]. When conjugated to a targeted ligand, the particles demonstrated tumor enhancement in a murine model.

Recently, a squared-shaped, PEG-coated, 24 nm, gadolinium-based nano-composite was synthesized for gastrointestinal tract imaging [85]. It presented a high longitudinal relaxivity value at 1.4 T ($r_1 = 16.4\ mM^{-1}s^{-1}$) and yielded distinct brightening of a rabbit stomach for more than an hour, after oral administration.

5.2.3 Manganese-Based Nanoparticles

In 2007, MnO nanoparticles of various sizes were reported as possible MRI T1 contrast agents [86]. The researchers synthesized particles of 7, 15, 20, and 25 nm in size and found that the r_1 values increased as the particles became smaller (maximal value of 0.37 $mM^{-1}s^{-1}$ at 3 T for the 7 nm agent). After injecting the particles to mice, the kidney contrast improved as well as the visualization of various brain structures. On a brain tumor model, nontargeted MnO particles yielded image brightening in various brain regions (attributed to impaired blood-brain barrier), whereas targeted MnO particles resulted in specific contrast enhancement in the tumor.

In a later study, the molar $r1$ relaxivity of MnO-based composites was increased ($0.99\ \text{mM}^{-1}\text{s}^{-1}$ at 11.7 T), by using mesoporous silica coating [87]. The authors hypothesized that the improved T1-related effect stems from the ability of water molecules to penetrate the coating. These particles (diameter = 86 nm) were used to label mesenchymal stem cells transplanted in mice brains and were ultimately visualized as a white dot in a T1-weighted scan.

A further improvement in r_1 value was later presented ($3.55\ \text{mM}^{-1}\text{s}^{-1}$), when yolk/shell hollow particles of manganese-based and platinum particles (40–50 nm core) were synthesized [88]. In vitro cell studies, however, revealed that the resulting composites are more cytotoxic than solid MnO particles.

Recently, a nano-scaled composite containing manganese and graphene, functionalized with dextran was synthesized [89]. It demonstrated a very high relaxivity value of $92\ \text{mM}^{-1}\text{s}^{-1}$. The blood vessels of mice were brightened for about 2 h post the NPs injection on 7 T magnetic field.

5.2.4 Iron Oxide-Based Nanoparticles

Iron oxide nanoparticles (IONPs) are characterized by an extremely high r_2 molar relaxivity value, rendering them excellent T2/T2* contrast agents. They are capable of altering image contrast even in relatively small concentrations. The common composites are magnetite (Fe_3O_4) and maghemite (γ-Fe_2O_3), but other variants are also under research [90].

Feridex®, a dextran-coated iron oxide nano-agent, was the first FDA-approved iron-based contrast agent [91] and was used for liver tumor detection. Iron is naturally taken by the liver Kupffer cells and macrophages in general [92]. When a liver pathology exists, the anomalous cell (as in a tumor or metastasis) does not contain macrophage-related activity; therefore the healthy parts of the liver are darkened when they absorb the IONPs, while the diseased region remains bright [93].

An important pathology that does involve macrophages' activity is inflammation. By injecting IONPs intravenously, their accumulation in inflamed regions can be detected. The utilization of this concept was demonstrated in an inflammatory bowel disease (IBD) rat model [94]. Using T2-weighed imaging after ultra-small (3–5 nm) IONPs IV injection, inflamed colon regions were well visualized and corresponded to histology findings. In a later work, IBD-induced mice were injected with macrophage-labeled IONPs. The particles manifested as reduced signal regions with an approximately 50% reduction at the intestine, and their visualization was strongly correlated with clinical score [95]. Other macrophage-related applications of IONPs include infection studies, renal inflammation, and heart conditions [96].

As stated earlier, the main and most significant effect of IONPs is T2/T2* shortening, which stems from creating local field inhomogeneity. The IONPs cause a susceptibility difference relative to their physiological surroundings. Such effect is manifested as image darkening, also termed as negative contrast (see Fig. 8.12). The disadvantage of this phenomenon is the difficulty in distinguishing IONPs' related dark regions, from natural image voids and artifacts. Nevertheless, several approaches were investigated for achieving IONPs' positive image contrast (brightened regions). To begin with, the transverse and longitudinal molar relaxivity

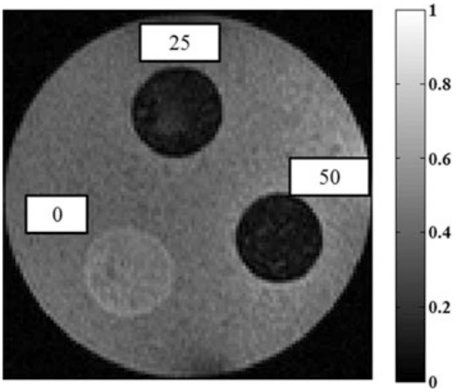

Fig. 8.12 An MRI image of IONPs phantom. The three equal-sized circles correspond to the IONPs target cylinders embedded in an agar phantom: control (no IONPs) region, 25 μg/mL IONPs region, and 50 μg/mL IONPs region. Note the substantial image darkening associated with the nanoparticles

values of the previously FDA-approved Feridex IONP-based contrast agents are 120 $\mathrm{mM}^{-1}\mathrm{s}^{-1}$ and 10.1 $\mathrm{mM}^{-1}\mathrm{s}^{-1}$, respectively [97]. As the r_2/r_1 ratio is higher than 10 in this case, the T2/T2* effect is mostly dominant. Ferumoxytol, on the other hand, is an FDA-approved iron supplement for anemia patients, with relaxivity values of $r_1 = 38\ \mathrm{mM}^{-1}\mathrm{s}^{-1}$ and $r_2 = 83\ \mathrm{mM}^{-1}\mathrm{s}^{-1}$ [98]. Given the smaller r_2/r_1 ratio in this case, the compound is useful for both T1 and T2 imaging, using T1-weighted and T2-weighted pulse sequences, respectively. Ferumoxytol was investigated for various angiography-related positive contrast applications [99]. It was found to provide distinct image brightening, as long as the particles are diluted enough, to prevent susceptibility-related, T2* artifacts (stemming from the high r_2 value). The capability of ferumoxytol in improving cancer detection in children and young adults was evaluated in a 22-subject human trial [100]. Whole-body diffusion-weighted images were fused with T1-weighted images after the IONP administration, yielding tumor detection and staging abilities, comparable to those of PET/CT.

Another approach for obtaining positive contrast using IONPs is using special MRI pulse sequences that will selectively excite the water surrounding the IONPs [101]. Using this approach, images depicting the IONPs' location only (visualized as white regions) can be obtained. Other proposed methods were based on post-processing of phase images [102] and ultrashort echo time [103].

Recently, selective positive contrast imaging of IONPs was suggested, using acoustically induced rotary saturation [104]. According to this approach, the imaged area is acoustically vibrated or displaced, while applying a modified spin-lock imaging protocol. The IONPs create a substantial susceptibility effect, yielding a change in the local field; hence, if displaced at the relevant frequency (with respect to the spin-lock frequency), they may produce a signal change, proportional to their concentration. The concept was demonstrated in phantoms, with 10 nm maghemite NPs. The minimal detected concentration was 20 μg/mL Fe, and the resulting images contained color overlay of the IONPs only, atop T2-weighted conventional images.

To summarize this section, a list of related NPs and their effect is outlined in Table 8.1.

Table 8.1 Recently published examples of MRI NPs research

Nanoparticle type	Clinical application (imaging target)	Core size (nm)	Additional study information	References
Gadolinium-based	Gastrointestinal tract	24	Rabbit study	[85]
	Kidney and liver	2.9	Gadolinium oxide NPs	[82]
	Tumor	12	Gadolinium-encapsulated carbon dots; mice study	[84]
	Brain therapy monitoring	–	Gadolinium-functionalized nanographene oxide, mice study	[105]
Iron-based	Tumor angiogenesis	5.14	Polymer-coated IONPs, mice study	[106]
	Tumor necrosis	Less than 30	Human study + mice study	[98]
	Tumor apoptosis	128.4	Magnetite aggregates	[107]
	Ovarian cancer	9.2	Folic acid targeting, mice	[108]
	Atherosclerosis	24	Zinc-doped ferrite nanoparticles, rat model	[109]
	Inflammatory bowel disease	3–5	Rat model	[94]
		–	Mice	[95]
	Brain tumors	30	Human study	[110]
	Alzheimer's disease	Less than 100	Mice study Curcumin-conjugated IONPs	[111]
	Lymph node	Less than 59	Human study	[112]
	Liver	22	Fe_5C_2 $r_2 \approx 973 \mathrm{mM}^{-1}\mathrm{s}^{-1}$	[113]
	Pancreatic cancer	110–130	$Fe_3O_4@SiO_2$ modified with anti-mesothelin antibody, mice study	[114]
		10.3	Mice study, milk protein-coated particles	[115]
Manganese-based	Monitoring apoptotic area in brain injury	–	Rats study	[116]
	Brain and kidney	7–25	Mice study $r_1 = 0.12 - 0.37\ \mathrm{mM}^{-1}\mathrm{s}^{-1}$	[86]
	Tumor	8	Mice study $r_1 \approx 0.6\ \mathrm{mM}^{-1}\mathrm{s}^{-1}$	[117]
		100	Mice study $r_1 \approx 10.2\ \mathrm{mM}^{-1}\mathrm{s}^{-1}$	[118]

(*continued*)

Table 8.1 (continued)

Nanoparticle type	Clinical application (imaging target)	Core size (nm)	Additional study information	References
Others	Liver	12	Combination of gadolinium, manganese and iron oxide, dual T1 and T2 contrast, mice study	[119]
	Cell labeling	Around 200	PLGA-perfluorooctyl bromide NPs, ^{19}F-MRI, mice study	[120]
	Venous thrombosis	Less than 165	Perfluorocarbon nanoemulsions, ^{19}F-MRI, mice study	[79]
	Brain tumors	5	CEST contrast agent, mice study	[80]

5.3 Nano-Scaled Compounds for Multimodal MRI-Ultrasound Imaging

Multimodal imaging, namely, the ability to image the same object with more than one imaging modality, is a rapidly growing field of research. A prominent example in terms of hardware is the usage of PET/CT scanners, which offers the ability to fuse metabolic and highly specific functional images with high-resolution anatomical images. In the field of nano-scaled contrast agents, the ability to use a single composite for more than one modality can significantly improve diagnosis certainty. As an illustration, consider IONPs which are administered to an MRI-scanned patient. In case a relatively high concentration of the IONPs reaches a diseased site, a dark image void may appear. To clinically ensure that the visualized darkening is not the result of a random artifact, a second image obtained by a modality which is based on a different physical process may provide a definitive answer. For example, if the IONPs could also generate a well-discernible image contrast in US as well as MRI, the patient could undergo two consecutive examinations if needed, confirming the suspected diagnosis.

The main research conducted in engineering nano-scaled complexes, capable of providing a dual-modal imaging by both MRI and US, can be divided into two main categories: (i) embedding an MRI metal-based, relaxation time-altering nano-agents, such as gadolinium-based, manganese-based, or iron-based, into a nano-scaled ultrasound contrast agent, such as nanobubble, nanodroplet, and ELIP, and (ii) attempting to find an “as-is” nano-agent which will be suitable for US imaging as well as MRI, without any required modifications.

5.3.1 Metal in Bubble Dual-Modal Composites

Initially, extensive research was conducted in attempting to trap the most commonly used MRI NPs – IONPs, in the most commonly used ultrasound contrast agent – namely, microbubbles [121, 122]. The resulting composite dimensions were in many cases larger than a micron. Although larger than the defined nano-scale, this type of agents will be shortly described here due to their impact on later detected nano-based complexes which provided dual-modal capability. One such example is the synthesis

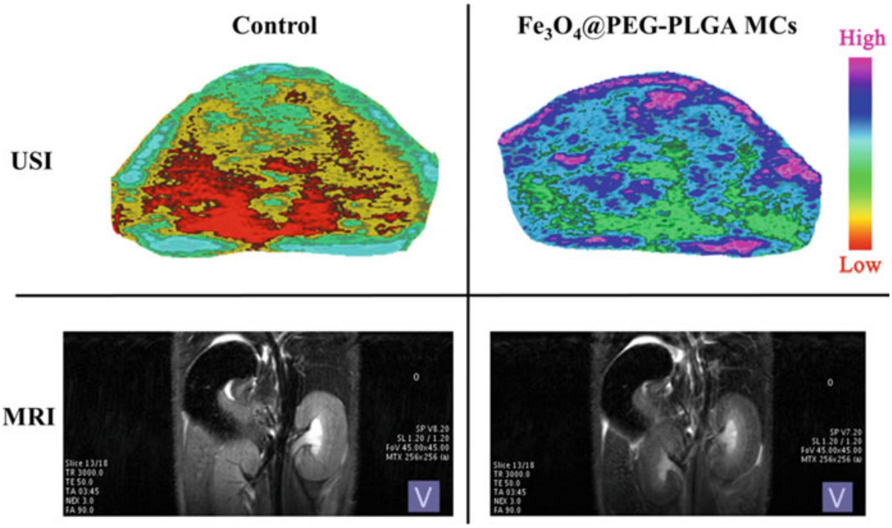

Fig. 8.13 In vivo ultrasound images of mouse liver (top) and MRI images of mouse kidneys (bottom), after injection of control saline (left) and Fe_3O_4@PEG-PLGA microcapsules (right). Generously contributed by Prof. Decheng Wu from the Institute of Chemistry, Chinese Academy of Sciences

of IONPs in a fluorocarbon gas core, polymer-shelled microbubbles [123]. The resulting complex size could be tuned between 450 and 1300 nm in size, but the ultrasound contrast was found to degrade as the size was reduced. The suitability of the composite for dual-modal imaging was demonstrated in rat livers. Although deviating from the scope of this chapter, it should be noted that one of the advantages of such bubble-based complexes is the capability to load them with therapeutic materials. For example, various studies embedded antitumor medications in bubbles [124]. Figure 8.13 depicts a representative example of iron oxide in microcapsules multimodal ultrasound-MRI study [122]. As can be noted, the administered complex agent results in both increased ultrasound echogenicity and MRI contrast alteration (commonly T2/T2*-related image darkening).

As mentioned earlier, the main limitation in the aforementioned complexes is the relatively large agent size, preventing efficient tumor accumulation. Several recent works succeeded, nonetheless, to obtain smaller contrast agent sizes. Huang et al. [125] synthesized bubbles with an approximate size of 200 nm. The outer shell was made of polyacrylic acid (PAA) and pluronic F127. The inner volume contained embedded iron oxide NPs and entrapped PFP gas. The nanobubbles demonstrated increased B-scan ultrasound contrast in vivo (subcutaneous tumor-bearing mouse), as well as MRI T2-shortening effect. The incorporation of IONPs to the nanobubbles demonstrated an improvement in the US contrast, with respect to gas-only bubbles. In addition, when a magnet was positioned next to the tumor, the nanobubbles presented improved selective accumulation.

In another work, IONPs were embedded in water instead of gas and encapsulated in a methoxy PEG-PLA shell [126]. An in vitro study has demonstrated that the acoustic attenuation increased with the IONPs concentration. By the same concept, other nano-size ultrasound contrast-enhancing complex types can be used to trap a magnetic nano-metal element, thus resulting in a multimodal imaging contrast agent. Based on the nanodroplet mechanism (see Sect. 5.1.3), IONPs were embedded in a polymer shell with a phase-changing liquid core [127]. As IONPs are sensitive to laser irradiation, near-infrared energy was used to convert the liquid core into gas and resulted in an acoustic contrast improvement, in addition to the T2-based MRI contrast. The concept was illustrated on mice livers and tumors. In another study, SPIO containing nano-droplets enhanced liver US-MRI signal, while the phase change from liquid core nanobubbles to gas core microbubbles was triggered using ultrasound [128].

Another example of ultrasonic agent embedded with metallic MRI agent is the combination of gadolinium with mesoporous silica NPs. The resulting 200 nm in size compound, demonstrated multimodal enhancing abilities for stem cells imaging [129].

5.3.2 Multimodal Solid Nanoparticles

Although the previously mentioned, bubble-like structure complexes resulted in noticeable MRI and US contrast improvement, they suffer from two main shortcomings: the complex size is typically larger than 100 nm, and the synthesis procedure may be complicated. These reasons motivated several studies, in which the suitability of the “as-is,” smaller than 100 nm, metallic nanoparticle with MRI and ultrasound imaging was examined. In a rat brain tumor model, animals were administered with IONPs and imaged using MRI (resulting in T2 image darkening). Next, ultrasound images of the ex vivo removed brains were taken, demonstrating brighter tumors when SPIO was administered (with respect to control or gadolinium administration) [130]. In a later similar study, ex vivo rat brain imaging after IONPs injection allowed improved visualization of the central nervous system (CNS) lesions, which corresponded to the detected locations on MRI [131]. In a later study, however, B-scan ultrasound of IONPs did not result in a satisfying and distinct contrast improvement [132].

Another method, developed for improving the ultrasonic detection ability of IONPs is magneto-motive ultrasound (MMUS) [133]. According to this approach, a magnetic generator is placed under the imaged organ. After IONPs injection and their arrival to the designated pathology-suspected area, the magnetic field vibrates the particles, which in turn can be detected by ultrasound. In a consecutive study, IONPs were detected in rats sentinel lymph nodes using MRI imaging in vivo and MMUS *postmortem* [134].

A different approach was recently suggested for IONPs ultrasonic detection. Since the underlying physical property of the conventional B-mode ultrasound (backscatter) was not sufficient for the particles unequivocal detection [132], the effect of the particles on other acoustic characteristics was examined [135]. The study found that IONPs do not affect the acoustic attenuation in a clinically relevant concentration range. However, they increased the speed of sound (SOS) of the examined object in a linear manner. This acoustic property can be imaged using the through-transmission ultrasound method (see Sect. 4.2). In a set of in vitro and ex vivo experiments, the feasibility of IONPs' detection via SOS change was demonstrated, while MRI of the same particles, with similar concentration, verified multimodal contrast capabilities.

Another type of "as-is" solid NPs suitable for both MRI and through-transmission ultrasound are copper oxide (CuO) NPs [136]. These 7 nm in diameter particles yielded T1-based contrast improvement on an agar-based phantom at 9.4 T while providing concentration-dependent through-transmission ultrasound enhancement. In contrary to IONPs, the dominant physical property affected by the CuO presence was the acoustic attenuation.

A summary of this section is outlined in Table 8.2.

Table 8.2 Recently published examples of multimodal US-MRI NPs studies

Nanoparticle type	Clinical application (imaging target)	Core size (nm)	Additional study information	References
IONPs in microbubble	Liver	400–1300	Rat study, polymer shell-encapsulating fluorocarbon gas and IONPs	[123]
	Liver, kidney, and spleen	3.7 micron	Magnetite in PEG-PLGA microcapsules, mice study	[122]
	Tumor	Larger than a micron	Maghemite in a polymer-based microbubble	[121]
	Tumor lymph node	868	A chemotherapeutic drug was also encapsulated	[124]
IONPs combined with US nano-agent	General imaging (in vitro study)	50–200	In vitro study, IONPs in liquid core, PEG-PLA-based shell	[126]
	Liver and tumor	374	IONPs embedded in the polymeric shell of a phase-changing liquid core, near-infrared irradiation activated	[127]
	Tumor	200	IONPs in polymeric thermo-sensitive nanobubble	[125]
	Liver	385	IONPs embedded in a nanodroplet, ultrasound shifted to a microbubble	[128]
Gadolinium combined with US nano-agent	Stem cells	200	Cardiac tissue enhancement after silica-Gd-nanoparticle-labeled stem cell injection, mice study	[129]
	Tumor	100–400	Hollow silica nanospheres combined with gadolinium, mice study	[137]

(*continued*)

Table 8.2 (continued)

Nanoparticle type	Clinical application (imaging target)	Core size (nm)	Additional study information	References
Multimodal solid NPs	Brain	62	Ex vivo rat brains imaged using SPIO on B-mode ultrasound and T2-weighted MRI	[130, 131]
	Kidney	87	Magneto-motive ultrasound of IONPs	[133]
	Sentinel lymph nodes	31 and 67	Magneto-motive ultrasound *postmortem* and MRI in vivo	[134]
	In vitro and ex vivo studies performed so far	7–10	Through-transmission ultrasound and MRI	[135, 136]
Others	Human pancreatic islets tracking	170–213	Perfluorocarbon NPs for ^{19}F MRI and US imaging	[138]

6 Conclusions and Future Perspective

The field of nano-scaled contrast agent development has attracted extensive and international research efforts. Nevertheless, the only FDA-approved and commercially available ultrasound/MRI nano-scaled contrast agent today is iron oxide [139]. Several main limitations hamper the bridge-crossing between the preclinical vast research effort and the clinical implementation: (i) the toxicity profile of the nano-agents has to be thoroughly defined and biocompatibility well proven [140] for obtaining regulatory approvals; (ii) for reproducibility, as slight changes in particle morphology may alter its efficiency and physiological behavior, the manufacturing process needs to be precisely repeated for each new batch [141]; and (iii) the targeting ability must be sufficient, namely, great percentages of the injected dose ultimately arriving the target site, allowing clear differentiation between healthy and pathological tissue.

Another obstacle, for de facto translation of a discovered nano-scaled contrast agent into a routine clinical practice use, is the “proof-of-concept” approach. In other words, the majority of studies provide an initial investigation of a newly developed material by means of in vitro cell cultures and most typically murine studies. However, once completed, no further investigations and consecutive research on larger animals/clinical trials are commonly conducted.

In terms of ultrasound nano-agents, it shall be noted that the majority of studies described relatively large materials, in many cases exceeding 500 nm. As the probability of benefiting from the associated EPR effect increases for smaller NPs [142], it is highly desirable to reduce the size of US-dedicated agents. In that sense, solid nanoparticles could provide a possible solution.

In summary, it should be noted that the fascinating multidisciplinary knowledge, integrated in the field of nano-scaled contrast agents, requires expertise in various fields. In the endeavor to obtain a major nano-progress, scientific multidisciplinary teamwork plays a critical role [31].

References

1. Wolbarst AB, Hendee WR (2006) Evolving and experimental technologies in medical imaging. Radiology 238(1):16–39
2. Smith-Bindman R, Miglioretti DL, Johnson E, Lee C et al (2012) Use of diagnostic imaging studies and associated radiation exposure for patients enrolled in large integrated health care systems, 1996–2010. JAMA 307(22):2400–2409
3. Beckett KR, Moriarity AK, Langer JM (2015) Safe use of contrast media: what the radiologist needs to know. Radiographics 35(6):1738–1750
4. Vandsburger MH, Epstein FH (2011) Emerging MRI methods in translational cardiovascular research. J Cardiovasc Transl Res 4(4):477–492
5. Fidler JL, Guimaraes L, Einstein DM (2009) MR imaging of the small bowel 1. Radiographics 29(6):1811–1825
6. Sun MR, Ngo L, Genega EM, Atkins MB et al (2009) Renal cell carcinoma: dynamic contrast-enhanced MR imaging for differentiation of tumor subtypes – correlation with pathologic findings 1. Radiology 250(3):793–802
7. Farkas J, Christian P, Urrea JAG, Roos N et al (2010) Effects of silver and gold nanoparticles on rainbow trout (*Oncorhynchus mykiss*) hepatocytes. Aquat Toxicol 96(1):44–52
8. Bihari P, Vippola M, Schultes S, Praetner M et al (2008) Optimized dispersion of nanoparticles for biological in vitro and in vivo studies. Part Fibre Toxicol 5(1):14
9. Mohanraj V, Chen Y (2006) Nanoparticles-a review. Trop J Pharm Res 5(1):561–573
10. Moreno-Manas M, Pleixats R (2003) Formation of carbon– carbon bonds under catalysis by transition-metal nanoparticles. Acc Chem Res 36(8):638–643
11. Kayser O, Lemke A, Hernandez-Trejo N (2005) The impact of nanobiotechnology on the development of new drug delivery systems. Curr Pharm Biotechnol 6(1):3–5
12. Wang AZ, Langer R, Farokhzad OC (2012) Nanoparticle delivery of cancer drugs. Annu Rev Med 63:185–198
13. Hobbs SK, Monsky WL, Yuan F, Roberts WG et al (1998) Regulation of transport pathways in tumor vessels: role of tumor type and microenvironment. Proc Natl Acad Sci 95(8):4607–4612
14. Fang J, Nakamura H, Maeda H (2011) The EPR effect: unique features of tumor blood vessels for drug delivery, factors involved, and limitations and augmentation of the effect. Adv Drug Deliv Rev 63(3):136–151
15. Li S-D, Huang L (2010) Stealth nanoparticles: high density but sheddable PEG is a key for tumor targeting. J Control Release 145(3):178
16. Moore A, Marecos E, Bogdanov A Jr, Weissleder R (2000) Tumoral distribution of long-circulating dextran-coated iron oxide nanoparticles in a rodent model 1. Radiology 214 (2):568–574
17. Nune SK, Gunda P, Thallapally PK, Lin Y-Y et al (2009) Nanoparticles for biomedical imaging. Expert Opin Drug Deliv 6(11):1175–1194
18. Li L, Gao F, Jiang W, Wu X et al (2016) Folic acid-conjugated superparamagnetic iron oxide nanoparticles for tumor-targeting MR imaging. Drug Deliv 23(5):1726–1733
19. Grenha A, Gomes ME, Rodrigues M, Santo VE et al (2010) Development of new chitosan/carrageenan nanoparticles for drug delivery applications. J Biomed Mater Res A 92(4):1265–1272
20. Alivisatos P (2004) The use of nanocrystals in biological detection. Nat Biotechnol 22(1):47–52

21. Zhou L, Gu Z, Liu X, Yin W et al (2012) Size-tunable synthesis of lanthanide-doped Gd_2O_3 nanoparticles and their applications for optical and magnetic resonance imaging. J Mater Chem 22(3):966–974
22. Zhao Z, Zhou Z, Bao J, Wang Z et al (2013) Octapod iron oxide nanoparticles as high-performance T2 contrast agents for magnetic resonance imaging. Nat Commun 4:2266
23. Baetke SC, Lammers T, Kiessling F (2015) Applications of nanoparticles for diagnosis and therapy of cancer. Br J Radiol 88(1054):20150207
24. Popovtzer R, Agrawal A, Kotov NA, Popovtzer A et al (2008) Targeted gold nanoparticles enable molecular CT imaging of cancer. Nano Lett 8(12):4593–4596
25. Yin T, Wang P, Zheng R, Zheng B et al (2012) Nanobubbles for enhanced ultrasound imaging of tumors. Int J Nanomedicine 7(2):895–904
26. Liu Y, Welch MJ (2012) Nanoparticles labeled with positron emitting nuclides: advantages, methods, and applications. Bioconjug Chem 23(4):671–682
27. Polyák A, Hajdu I, Bodnár M, Trencsényi G et al (2013) 99m Tc-labelled nanosystem as tumour imaging agent for SPECT and SPECT/CT modalities. Int J Pharm 449(1):10–17
28. Morana G, Salviato E, Guarise A (2007) Contrast agents for hepatic MRI. Cancer Imaging 7 (Spec No A):S24–S27
29. Louie A (2010) Multimodality imaging probes: design and challenges. Chem Rev (Washington, DC, United States) 110(5):3146–3195
30. Deshpande N, Needles A, Willmann JK (2010) Molecular ultrasound imaging: current status and future directions. Clin Radiol 65(7):567–581
31. Gao Z, Ma T, Zhao E, Docter D et al (2016) Small is smarter: nano MRI contrast agents–advantages and recent achievements. Small 12(5):556–576
32. Lee D-E, Koo H, Sun I-C, Ryu JH et al (2012) Multifunctional nanoparticles for multimodal imaging and theragnosis. Chem Soc Rev 41(7):2656–2672
33. Albrecht T, Blomley M, Bolondi L, Claudon M et al (2004) Guidelines for the use of contrast agents in ultrasound. January 2004. Ultraschall Med 25(04):249–256
34. Chang PH, Shun K, Wu S-J, Levene HB (1995) Second harmonic imaging and harmonic Doppler measurements with Albunex. IEEE Trans Ultrason Ferroelectr Freq Control 42(6):1020–1027
35. Calliada F, Campani R, Bottinelli O, Bozzini A et al (1998) Ultrasound contrast agents: basic principles. Eur J Radiol 27:S157–S160
36. Blomley MJ, Cooke JC, Unger EC, Monaghan MJ et al (2001) Microbubble contrast agents: a new era in ultrasound. Br Med J 322(7296):1222
37. Potdevin T, Fowlkes J, Moskalik A, Carson P (2004) Analysis of refill curve shape in ultrasound contrast agent studies. Med Phys 31(3):623–632
38. Claudon M, Dietrich CF, Choi BI, Cosgrove DO et al (2013) Guidelines and good clinical practice recommendations for contrast enhanced ultrasound (CEUS) in the liver–update 2012. Ultraschall Med 34(01):11–29
39. Wang C-H, Huang Y-F, Yeh C-K (2011) Aptamer-conjugated nanobubbles for targeted ultrasound molecular imaging. Langmuir 27(11):6971–6976
40. Fan X, Wang L, Guo Y, Tong H et al (2013) Experimental investigation of the penetration of ultrasound nanobubbles in a gastric cancer xenograft. Nanotechnology 24(32):325102
41. Cai WB, Yang HL, Zhang J, Yin JK et al (2015) The optimized fabrication of nanobubbles as ultrasound contrast agents for tumor imaging. Sci Rep 5:13725
42. Yang H, Cai W, Xu L, Lv X et al (2015) Nanobubble–affibody: novel ultrasound contrast agents for targeted molecular ultrasound imaging of tumor. Biomaterials 37:279–288
43. Tong H-P, Wang L-F, Guo Y-L, Li L et al (2013) Preparation of protamine cationic nanobubbles and experimental study of their physical properties and in vivo contrast enhancement. Ultrasound Med Biol 39(11):2147–2157
44. Makadia HK, Siegel SJ (2011) Poly lactic-co-glycolic acid (PLGA) as biodegradable controlled drug delivery carrier. Polymers 3(3):1377–1397
45. Néstor M-M, Kei N-PE, Guadalupe N-AM, Elisa M-ES et al (2011) Preparation and in vitro evaluation of poly (D, L-lactide-co-glycolide) air-filled nanocapsules as a contrast agent for ultrasound imaging. Ultrasonics 51(7):839–845

46. Zhang X, Zheng Y, Wang Z, Huang S et al (2014) Methotrexate-loaded PLGA nanobubbles for ultrasound imaging and synergistic targeted therapy of residual tumor during HIFU ablation. Biomaterials 35(19):5148–5161
47. Krupka TM, Solorio L, Wilson RE, Wu H et al (2009) Formulation and characterization of echogenic lipid– pluronic nanobubbles. Mol Pharm 7(1):49–59
48. Wu H, Rognin NG, Krupka TM, Solorio L et al (2013) Acoustic characterization and pharmacokinetic analyses of new nanobubble ultrasound contrast agents. Ultrasound Med Biol 39(11):2137–2146
49. Shapiro MG, Goodwill PW, Neogy A, Yin M et al (2014) Biogenic gas nanostructures as ultrasonic molecular reporters. Nat Nanotechnol 9(4):311–316
50. Sheeran PS, Wong VP, Luois S, McFarland RJ et al (2011) Decafluorobutane as a phase-change contrast agent for low-energy extravascular ultrasonic imaging. Ultrasound Med Biol 37 (9):1518–1530
51. Díaz-López R, Tsapis N, Santin M, Bridal SL et al (2010) The performance of PEGylated nanocapsules of perfluorooctyl bromide as an ultrasound contrast agent. Biomaterials 31(7):1723–1731
52. Peyman SA, McLaughlan JR, Abou-Saleh RH, Marston G et al (2016) On-chip preparation of nanoscale contrast agents towards high-resolution ultrasound imaging. Lab Chip 16(4):679–687
53. Liu J, Shang T, Wang F, Cao Y et al (2017) Low-intensity focused ultrasound (LIFU)-induced acoustic droplet vaporization in phase-transition perfluoropentane nanodroplets modified by folate for ultrasound molecular imaging. Int J Nanomedicine 12:911
54. Nguyen AT, Wrenn SP (2014) Acoustically active liposome-nanobubble complexes for enhanced ultrasonic imaging and ultrasound-triggered drug delivery. Wiley Interdiscip Rev Nanomed Nanobiotechnol 6(3):316–325
55. Raymond JL, Luan Y, Peng T, Huang S-L et al (2016) Loss of gas from echogenic liposomes exposed to pulsed ultrasound. Phys Med Biol 61(23):8321
56. Liang H, Blomley M (2003) The role of ultrasound in molecular imaging. Br J Radiol 76:S140
57. Kopechek JA, Haworth KJ, Raymond JL, Douglas Mast T et al (2011) Acoustic characterization of echogenic liposomes: frequency-dependent attenuation and backscatter. J Acoust Soc Am 130(5):3472–3481
58. Radhakrishnan K, Haworth KJ, Huang S-L, Klegerman ME et al (2012) Stability of echogenic liposomes as a blood pool ultrasound contrast agent in a physiologic flow phantom. Ultrasound Med Biol 38(11):1970–1981
59. Kim H, Moody MR, Laing ST, Kee PH et al (2010) In vivo volumetric intravascular ultrasound visualization of early/inflammatory arterial atheroma using targeted echogenic immunoliposomes. Investig Radiol 45(10):685
60. Laing ST, Moody M, Smulevitz B, Kim H et al (2011) Ultrasound-enhanced thrombolytic effect of tissue plasminogen activator–loaded echogenic liposomes in an in vivo rabbit aorta thrombus model – brief report. Arterioscler Thromb Vasc Biol 31(6):1357–1359
61. Kang E, Min HS, Lee J, Han MH et al (2010) Nanobubbles from gas-generating polymeric nanoparticles: ultrasound imaging of living subjects. Angew Chem Int Ed 49(3):524–528
62. Olson ES, Orozco J, Wu Z, Malone CD et al (2013) Toward in vivo detection of hydrogen peroxide with ultrasound molecular imaging. Biomaterials 34(35):8918–8924
63. Kang C, Cho W, Park M, Kim J et al (2016) H_2O_2-triggered bubble generating antioxidant polymeric nanoparticles as ischemia/reperfusion targeted nanotheranostics. Biomaterials 85:195–203
64. Kim M, Lee JH, Kim SE, Kang SS et al (2016) Nanosized ultrasound enhanced-contrast agent for in vivo tumor imaging via intravenous injection. ACS Appl Mater Interfaces 8(13):8409–8418
65. Liu J, Levine AL, Mattoon JS, Yamaguchi M et al (2006) Nanoparticles as image enhancing agents for ultrasonography. Phys Med Biol 51(9):2179
66. Liu J, Li J, Rosol TJ, Pan X et al (2007) Biodegradable nanoparticles for targeted ultrasound imaging of breast cancer cells in vitro. Phys Med Biol 52(16):4739

67. Ji Y, Li X-T, Chen G-Q (2008) Interactions between a poly (3-hydroxybutyrate-co-3-hydroxyvalerate-co-3-hydroxyhexanoate) terpolyester and human keratinocytes. Biomaterials 29(28):3807–3814
68. Liberman A, Martinez HP, Ta CN, Barback CV et al (2012) Hollow silica and silica-boron nano/microparticles for contrast-enhanced ultrasound to detect small tumors. Biomaterials 33(20):5124–5129
69. Liberman A, Wu Z, Barback CV, Viveros R et al (2013) Color doppler ultrasound and gamma imaging of intratumorally injected 500 nm iron–silica nanoshells. ACS Nano 7(7):6367–6377
70. Foroutan F, Jokerst JV, Gambhir SS, Vermesh O et al (2015) Sol–gel synthesis and electrospraying of biodegradable (P_2O_5) 55–(CaO) 30–(Na_2O) 15 glass nanospheres as a transient contrast agent for ultrasound stem cell imaging. ACS Nano 9(2):1868–1877
71. Delogu LG, Vidili G, Venturelli E, Ménard-Moyon C et al (2012) Functionalized multiwalled carbon nanotubes as ultrasound contrast agents. Proc Natl Acad Sci 109(41):16612–16617
72. Lee GH, Chang Y (2015) Magnetic properties, water proton relaxivities, and in-vivo MR images of paramagnetic nanoparticles. J Korean Phys Soc 67(1):44–51
73. Weissleder R (1994) Liver MR imaging with iron oxides: toward consensus and clinical practice. Radiology 193(3):593–595
74. Raymond KN, Pierre VC (2005) Next generation, high relaxivity gadolinium MRI agents. Bioconjug Chem 16(1):3–8
75. Kuo PH, Kanal E, Abu-Alfa AK, Cowper SE (2007) Gadolinium-based MR contrast agents and nephrogenic systemic fibrosis 1. Radiology 242(3):647–649
76. Pan D, Caruthers SD, Senpan A, Schmieder AH et al (2011) Revisiting an old friend: manganese-based MRI contrast agents. Wiley Interdiscip Rev Nanomed Nanobiotechnol 3(2):162–173
77. Amsalem Y, Mardor Y, Feinberg MS, Landa N et al (2007) Iron-oxide labeling and outcome of transplanted mesenchymal stem cells in the infarcted myocardium. Circulation 116(Suppl 11): I-38–I-45
78. Bar-Shir A, Avram L, Yariv-Shoushan S, Anaby D et al (2014) Alginate-coated magnetic nanoparticles for noninvasive MRI of extracellular calcium. NMR Biomed 27(7):774–783
79. Temme S, Grapentin C, Quast C, Jacoby C et al (2015) Non-invasive imaging of early venous thrombosis by 19F MRI using targeted perfluorocarbon nanoemulsions. Circulation. https://doi.org/10.1161/CIRCULATIONAHA.114.010962
80. Lesniak WG, Oskolkov N, Song X, Lal B et al (2016) Salicylic acid conjugated dendrimers are a tunable, high performance CEST MRI NanoPlatform. Nano Lett 16(4):2248–2253
81. Faucher L, Tremblay Ml, Lagueux J, Gossuin Y et al (2012) Rapid synthesis of PEGylated ultrasmall gadolinium oxide nanoparticles for cell labeling and tracking with MRI. ACS Appl Mater Interfaces 4(9):4506–4515
82. Fang J, Chandrasekharan P, Liu X-L, Yang Y et al (2014) Manipulating the surface coating of ultra-small Gd_2O_3 nanoparticles for improved T 1-weighted MR imaging. Biomaterials 35(5):1636–1642
83. Bertini I, Bianchini F, Calorini L, Colagrande S et al (2004) Persistent contrast enhancement by sterically stabilized paramagnetic liposomes in murine melanoma. Magn Reson Med 52(3):669–672
84. Chen H, Wang GD, Tang W, Todd T et al (2014) Gd-encapsulated carbonaceous dots with efficient renal clearance for magnetic resonance imaging. Adv Mater (Weinheim, Germany) 26(39):6761–6766
85. Perera VS, Chen G, Cai Q, Huang SD (2016) Nanoparticles of gadolinium-incorporated Prussian blue with PEG coating as an effective oral MRI contrast agent for gastrointestinal tract imaging. Analyst 141(6):2016
86. Na HB, Lee JH, An K, Park YI et al (2007) Development of a T1 contrast agent for magnetic resonance imaging using MnO nanoparticles. Angew Chem 119(28):5493–5497
87. Kim T, Momin E, Choi J, Yuan K et al (2011) Mesoporous silica-coated hollow manganese oxide nanoparticles as positive T 1 contrast agents for labeling and MRI tracking of adipose-derived mesenchymal stem cells. J Am Chem Soc 133(9):2955–2961
88. An K, Na HB, Park YI, Choi SH et al (2015) Hollow MnOxPy and Pt/MnOxPy yolk/shell nanoparticles as a T 1 MRI contrast agent. J Colloid Interface Sci 439:134–138

89. Kanakia S, Toussaint J, Hoang DM, Lee S et al (2014) Towards an advanced graphene-based magnetic resonance imaging contrast agent: sub-acute toxicity and efficacy studies in small animals. Sci Rep 5:17182–17182
90. Bao G, Mitragotri S, Tong S (2013) Multifunctional nanoparticles for drug delivery and molecular imaging. Annu Rev Biomed Eng 15:253–282
91. Wu Y, Briley K, Tao X (2015) Nanoparticle-based imaging of inflammatory bowel disease. Wiley Interdiscip Rev Nanomed Nanobiotechnol 8:300–315
92. Raynal I, Prigent P, Peyramaure S, Najid A et al (2004) Macrophage endocytosis of superparamagnetic iron oxide nanoparticles: mechanisms and comparison of ferumoxides and ferumoxtran-10. Investig Radiol 39(1):56–63
93. Van Beers B, Gallez B, Pringot J (1997) Contrast-enhanced MR imaging of the liver. Radiology 203(2):297–306
94. Frericks BB, Wacker F, Loddenkemper C, Valdeig S et al (2009) Magnetic resonance imaging of experimental inflammatory bowel disease: quantitative and qualitative analyses with histopathologic correlation in a rat model using the ultrasmall iron oxide SHU 555 C. Investig Radiol 44(1):23–30
95. Wu Y, Briley-Saebo K, Xie J, Zhang R et al (2014) Inflammatory bowel disease: MR-and SPECT/CT-based macrophage imaging for monitoring and evaluating disease activity in experimental mouse model – pilot study. Radiology 271(2):400–407
96. Neuwelt A, Sidhu N, Hu C-AA, Mlady G et al (2015) Iron-based superparamagnetic nanoparticle contrast agents for MRI of infection and inflammation. Am J Roentgenol 204(3): W302–W313
97. Aryal S, Key J, Stigliano C, Ananta JS et al (2013) Engineered magnetic hybrid nanoparticles with enhanced relaxivity for tumor imaging. Biomaterials 34(31):7725–7732
98. Aghighi M, Golovko D, Ansari C, Marina NM et al (2015) Imaging tumor necrosis with ferumoxytol. PLoS One 10(11):e0142665
99. Bashir MR, Bhatti L, Marin D, Nelson RC (2015) Emerging applications for ferumoxytol as a contrast agent in MRI. J Magn Reson Imaging 41(4):884–898
100. Klenk C, Gawande R, Uslu L, Khurana A et al (2014) Ionising radiation-free whole-body MRI versus 18 F-fluorodeoxyglucose PET/CT scans for children and young adults with cancer: a prospective, non-randomised, single-centre study. Lancet Oncol 15(3):275–285
101. Cunningham CH, Arai T, Yang PC, McConnell MV et al (2005) Positive contrast magnetic resonance imaging of cells labeled with magnetic nanoparticles. Magn Reson Med 53(5):999–1005
102. Zhao Q, Langley J, Lee S, Liu W (2011) Positive contrast technique for the detection and quantification of superparamagnetic iron oxide nanoparticles in MRI. NMR Biomed 24(5):464–472
103. Wang L, Zhong X, Qian W, Huang J et al (2014) Ultrashort echo time (UTE) imaging of receptor targeted magnetic iron oxide nanoparticles in mouse tumor models. J Magn Reson Imaging 40(5):1071–1081
104. Zhu B, Witzel T, Jiang S, Huang SY et al (2016) Selective magnetic resonance imaging of magnetic nanoparticles by acoustically induced rotary saturation. Magn Reson Med 75(1):97–106
105. Yang H-W, Huang C-Y, Lin C-W, Liu H-L et al (2014) Gadolinium-functionalized nanographene oxide for combined drug and microRNA delivery and magnetic resonance imaging. Biomaterials 35(24):6534–6542
106. Cui Y, Zhang C, Luo R, Liu H et al (2016) Noninvasive monitoring of early antiangiogenic therapy response in human nasopharyngeal carcinoma xenograft model using MrI with rgD-conjugated ultrasmall superparamagnetic iron oxide nanoparticles. Int J Nanomedicine 11:5671
107. Yuan Y, Ding Z, Qian J, Zhang J et al (2016) Casp3/7-instructed intracellular aggregation of Fe_3O_4 nanoparticles enhances T2 MR imaging of tumor apoptosis. Nano Lett 16(4):2686–2691
108. Zhang H, Li J, Hu Y, Shen M et al (2016) Folic acid-targeted iron oxide nanoparticles as contrast agents for magnetic resonance imaging of human ovarian cancer. J Ovarian Res 9(1):19

109. Chaudhary R, Roy K, Kanwar RK, Walder K et al (2016) Engineered atherosclerosis-specific zinc ferrite nanocomplex-based MRI contrast agents. J Nanobiotechnol 14(1):6
110. Dósa E, Guillaume DJ, Haluska M, Lacy CA et al (2010) Magnetic resonance imaging of intracranial tumors: intra-patient comparison of gadoteridol and ferumoxytol. Neuro Oncol 13:251. https://doi.org/10.1093/neuonc/noq172
111. Cheng KK, Chan PS, Fan S, Kwan SM et al (2015) Curcumin-conjugated magnetic nanoparticles for detecting amyloid plaques in Alzheimer's disease mice using magnetic resonance imaging (MRI). Biomaterials 44:155–172
112. Pouw JJ, Grootendorst MR, Bezooijen R, Klazen CA et al (2015) Pre-operative sentinel lymph node localization in breast cancer with superparamagnetic iron oxide MRI: the SentiMAG multicentre trial imaging subprotocol. Br J Radiol 88(1056):20150634
113. Cowger TA, Tang W, Zhen Z, Hu K et al (2015) Casein-coated Fe_5C_2 nanoparticles with superior r2 relaxivity for liver-specific magnetic resonance imaging. Theranostics 5(11):1225
114. Liu F, Le W, Mei T, Wang T et al (2016) In vitro and in vivo targeting imaging of pancreatic cancer using a Fe_3O_4@ SiO_2 nanoprobe modified with anti-mesothelin antibody. Int J Nanomedicine 11:2195
115. Huang J, Qian W, Wang L, Wu H et al (2016) Functionalized milk-protein-coated magnetic nanoparticles for MRI-monitored targeted therapy of pancreatic cancer. Int J Nanomedicine 11:3087
116. Jeon TY, Kim JH, Im GH, Kim J-H et al (2016) Hollow manganese oxide nanoparticle-enhanced MRI of hypoxic-ischaemic brain injury in the neonatal rat. Br J Radiol 89(1067):20150806
117. Luo Y, Yang J, Li J, Yu Z et al (2015) Facile synthesis and functionalization of manganese oxide nanoparticles for targeted T1-weighted tumor MR imaging. Colloids Surf B: Biointerfaces 136:506–513
118. Huang H, Yue T, Xu K, Golzarian J et al (2015) Fabrication and evaluation of tumor-targeted positive MRI contrast agent based on ultrasmall MnO nanoparticles. Colloids Surf B: Biointerfaces 131:148–154
119. Kuo Y-T, Chen C-Y, Liu G-C, Wang Y-M (2016) Development of bifunctional gadolinium-labeled superparamagnetic nanoparticles (Gd-MnMEIO) for in vivo MR imaging of the liver in an animal model. PLoS One 11(2):e0148695
120. Vu-Quang H, Vinding MS, Xia D, Nielsen T et al (2016) Chitosan-coated poly (lactic-co-glycolic acid) perfluorooctyl bromide nanoparticles for cell labeling in 19 F magnetic resonance imaging. Carbohydr Polym 136:936–944
121. Duan L, Yang F, Song L, Fang K et al (2015) Controlled assembly of magnetic nanoparticles on microbubbles for multimodal imaging. Soft Matter 11(27):5492–5500
122. Xu S, Yang F, Zhou X, Zhuang Y et al (2015) Uniform PEGylated PLGA microcapsules with embedded Fe_3O_4 nanoparticles for US/MR dual-modality imaging. ACS Appl Mater Interfaces 7(36):20460–20468
123. Song S, Guo H, Jiang Z, Jin Y et al (2015) Self-assembled microbubbles as contrast agents for ultrasound/magnetic resonance dual-modality imaging. Acta Biomater 24:266–278
124. Niu C, Wang Z, Lu G, Krupka TM et al (2013) Doxorubicin loaded superparamagnetic PLGA-iron oxide multifunctional microbubbles for dual-mode US/MR imaging and therapy of metastasis in lymph nodes. Biomaterials 34(9):2307–2317
125. Huang H-Y, Hu S-H, Hung S-Y, Chiang C-S et al (2013) SPIO nanoparticle-stabilized PAA-F127 thermosensitive nanobubbles with MR/US dual-modality imaging and HIFU-triggered drug release for magnetically guided in vivo tumor therapy. J Control Release 172(1):118–127
126. Xu B, Dou H, Tao K, Sun K et al (2011) "Two-in-one" fabrication of Fe_3O_4/MePEG-PLA composite nanocapsules as a potential ultrasonic/MRI dual contrast agent. Langmuir 27(19):12134–12142
127. Zhao Y, Song W, Wang D, Ran H et al (2015) Phase-shifted PFH@ PLGA/Fe_3O_4 nanocapsules for MRI/US imaging and photothermal therapy with near-infrared irradiation. ACS Appl Mater Interfaces 7(26):14231–14242

128. Cheng X, Li H, Chen Y, Luo B et al (2013) Ultrasound-triggered phase transition sensitive magnetic fluorescent nanodroplets as a multimodal imaging contrast agent in rat and mouse model. PLoS One 8(12):e85003
129. Kempen PJ, Greasley S, Parker KA, Campbell JL et al (2015) Theranostic mesoporous silica nanoparticles biodegrade after pro-survival drug delivery and ultrasound/magnetic resonance imaging of stem cells. Theranostics 5(6):631
130. Nolte I, Vince GH, Maurer M, Herbold C et al (2005) Iron particles enhance visualization of experimental gliomas with high-resolution sonography. Am J Neuroradiol 26 (6):1469–1474
131. Linker R, Kroner A, Horn T, Gold R et al (2006) Iron particle–enhanced visualization of inflammatory central nervous system lesions by high resolution: preliminary data in an animal model. Am J Neuroradiol 27(6):1225–1229
132. Oh J, Feldman MD, Kim J, Condit C et al (2006) Detection of magnetic nanoparticles in tissue using magneto-motive ultrasound. Nanotechnology 17(16):4183
133. Mehrmohammadi M, Oh J, Mallidi S, Emelianov SY (2011) Pulsed magneto-motive ultrasound imaging using ultrasmall magnetic nanoprobes. Mol Imaging 10(2):102. https://doi.org/10.2310/7290.2010.00037
134. Evertsson M, Kjellman P, Cinthio M, Fredriksson S et al (2014) Multimodal detection of iron oxide nanoparticles in rat lymph nodes using magnetomotive ultrasound imaging and magnetic resonance imaging. IEEE Trans Ultrason Ferroelectr Freq Control 61(8):1276–1283
135. Perlman O, Azhari H (2017) Ultrasonic computed tomography imaging of iron oxide nanoparticles. Phys Med Biol 62(3):825
136. Perlman O, Weitz IS, Azhari H (2015) Copper oxide nanoparticles as contrast agents for MRI and ultrasound dual-modality imaging. Phys Med Biol 60(15):5767
137. An L, Hu H, Du J, Wei J et al (2014) Paramagnetic hollow silica nanospheres for in vivo targeted ultrasound and magnetic resonance imaging. Biomaterials 35(20):5381–5392
138. Barnett BP, Ruiz-Cabello J, Hota P, Ouwerkerk R et al (2011) Use of perfluorocarbon nanoparticles for non-invasive multimodal cell tracking of human pancreatic islets. Contrast Media Mol Imaging 6(4):251–259
139. Thakor AS, Jokerst JV, Ghanouni P, Campbell JL et al (2016) Clinically approved nanoparticle imaging agents. J Nucl Med 57(12):1833–1837
140. Scheinberg DA, Grimm J, Heller DA, Stater EP et al (2017) Advances in the clinical translation of nanotechnology. Curr Opin Biotechnol 46:66–73
141. Kiessling F, Mertens ME, Grimm J, Lammers T (2014) Nanoparticles for imaging: top or flop? Radiology 273(1):10–28
142. Gu FX, Karnik R, Wang AZ, Alexis F et al (2007) Targeted nanoparticles for cancer therapy. Nano Today 2(3):14–21